TÜBİTAK

Turkish Journal of Physics

http://journals.tubitak.gov.tr/physics/

Review Article

Turk J Phys
(2014) 38: 478 – 496
© TÜBİTAK
doi:10.3906/fiz-1407-16

Two-dimensional MoS_2 as a new material for electronic devices

Natalia IZYUMSKAYA[1,*], Denis O. DEMCHENKO[2], Vitaliy AVRUTIN[1], Ümit ÖZGÜR[1], Hadis MORKOÇ[1]

[1]Department of Electrical and Computer Engineering, Virginia Commonwealth University, Richmond, Virginia, USA
[2]Department of Physics, Virginia Commonwealth University, Richmond, Virginia, USA

Received: 14.07.2014 • **Accepted:** 04.08.2014 • **Published Online:** 10.11.2014 • **Printed:** 28.11.2014

Abstract: We overview fundamental properties, preparation techniques, and potential device applications of single- and few-monolayer-thick molybdenum disulfide MoS_2 belonging to a new emerging class of materials: 2-dimensional semiconductors. To a large extent, the interest in the 2-dimensional materials is fueled by the quest for alternatives to graphene, which is hardly suitable for electronic devices because of the lack of a band gap. A unique combination of physical properties, including flexibility, high electron mobility, and optical transparency combined with a large band gap tunable from indirect 1.2 eV for bulk to direct 1.9 eV for a monolayer, make MoS_2 attractive for a variety of electronic and optoelectronic devices. The first device demonstrations are very encouraging: field-effect transistors with high current ON/OFF ratios, high-sensitivity phototransistors, logic circuits, and amplifiers based on monolayer-MoS_2 have been demonstrated. The layered structure of MoS_2 with other transition-metal dichalcogenides (WS_2, WSe_2, $MoSe_2$, etc.) makes it possible to grow ultrathin, so-called van der Waals heterostructures with very abrupt interfaces and low defect density and paves the way for fabricating multilayered materials for novel electronic and optical devices. However, further progress towards potential commercialization of monolayer-MoS_2-based devices requires serious efforts in the development of scalable fabrication techniques capable of producing large-area electronic-quality material.

Key words: Transition-metal dichalcogenide, molybdenum disulfide MoS_2, 2-dimensional semiconductor, exfoliation, chemical vapor deposition, field-effect transistor, van der Waals heterostructures

1. Introduction

The interest in 2-dimensional (2D) semiconductors is to a large extent fuelled by the highly successful miniaturization of Si-based electronic devices for higher packing density, faster circuit speed, and lower power dissipation. However, this long miniaturization drive extending existing material systems is approaching the physical limit for their operation. The new awareness of graphene [1] with its unique properties has aroused considerable interest in 2D semiconductors and their potential use in electronics and mechanical systems. Unfortunately, graphene appears to be hardly suitable for device applications because of the lack of band gap and, consequently, inability to switch off field-effect transistors (FETs) based on this material [2]. Therefore, other 2D materials, particularly the monolayer varieties, are emerging as a new class of materials with a wide range of electrical properties and potential practical applications. Among them are insulating BN [3] and semiconducting MoS_2 [4,5] and WSe_2 [6,7] , which are gaining increasing attention as promising channel materials and gate insulators for FETs. Molybdenum disulfide (MoS_2) and related materials, such as tungsten disulfide, as well as Mo and

*Correspondence: nizioumskaia@vcu.edu

W diselenides, are important members of the layered transition-metal dichalcogenides (TMDs) [8] and have attracted a good deal of attention recently because, as alluded to above, of their useful electronic and mechanical properties [9–11]. These materials have band gaps in the visible or near-infrared region of the electromagnetic spectrum and reportedly have potential applications as building blocks in even solar cells [11]. Furthermore, the layered crystal structure of these materials allows tuning of their electronic properties by either doping between weakly bonded layers or fabricating thin nanostructured materials [12–15].

Among TMDs, 2D MoS_2 offers a great promise for device applications. Excellent gate control, saturation, scalability, high current capability, and very low noise are among the expected salient features. Single-layer MoS_2 is a semiconductor with wide direct band gap, exhibits good electrical and transport properties, and is chemically and thermally stable, transparent, flexible, and relatively inexpensive, which all together make this material an excellent candidate for a variety of electronic and optoelectronic applications. The electronic structure of the MoS_2 single layers differs drastically from that of the bulk material. Bulk MoS_2 has an indirect band gap of 1.2 eV [16], a conduction band minimum (CBM) between the Γ and K points, and a valence band maximum (VBM) at the Γ point [17]. On the other hand, MoS_2 in the single-layer form exhibits a direct band gap [13,18–25] of 1.8–1.9 eV [13] with CBM and VBM at the K-point as a result of quantum confinement [20] and change in the symmetry. The band gap of MoS_2 can be tuned from 1.2 eV (bulk and indirect) up to 1.9 eV (monolayer and direct) by varying the number of monolayers [18], alloying (e.g., $Mo_xW_{1-x}S_2$) [26], or forming heterojunctions such as MoS_2/WS_2 [27]. Because the monolayer MoS_2 has a sizeable band gap, MoS_2-based FETs can be turned off [5,28]. These transistors demonstrate a current ON/OFF ratio of $\sim 1 \times 10^8$, low subthreshold swing (74 mV dec^{-1}), and negligible OFF current (25 fA μm^{-1}) [5]. Logic circuits [29,30] and amplifiers [31] based on monolayer MoS_2 have also been demonstrated, as well as good output current saturation and high currents [32].

There are many comprehensive reviews on transition-metal dichalcogenides [33–35]. In this contribution, we restrict our consideration to MoS_2 as it is, in our opinion, the most promising member of the TMD class of materials.

2. Properties of MoS_2

MoS_2 belongs to the group of TMDs with the common formula MX_2, wherein M represents a transition metal (M = Mo, W, Nb, Ta, Ti, Re, etc.) and X represents a chalcogen (X = Se, S or Te). The metal and chalcogen atoms have the oxidation states of +4 and –2, respectively. The crystal structure of bulk MoS_2 is formed by vertically stacked 2D layers with strong covalent bonding between atoms within a given layer and very weak van der Waals bonding between the adjacent layers. Within a single X-M-X layer, the M and X atoms form a 2D hexagonal sublattice. Depending on the stacking sequence along the hexagonal c axis, a number of structural polytypes are possible. Natural MoS_2 crystals with the trigonal prismatic (2H) and rhombohedral (3R) phases are common, the 2H trigonal prismatic being the most widespread [36]. In 1923, Dickinson and Pauling [37] first determined?the crystal structure of the 2H-MoS_2 polytype, known as molybdenite. Figure 1 shows the structure of bulk MoS_2 crystal. Each layer, 6.5 Å thick, consists of a plane of hexagonally packed Mo atoms sandwiched between 2 S atom planes. The structure belongs to the space group $P6_3/mmc$ (trigonal prism). The lattice parameters of bulk MoS_2 are a = 3.15 and c = 12.3 Å [38]. Depending of the Mo atom coordination, single layers of MoS_2 can exist in 2 polytypes: trigonal prismatic (D_{3h} point group, or $\overline{6}2m$ in the international notation) and octahedral (D_{3d} point group, or $\overline{3}2/m$) [39], as illustrated in Figure 2. The

semiconducting trigonal prismatic phase is thermodynamically stable, while the metallic octahedral phase is unstable and can be formed upon, for example, Li intercalation [40].

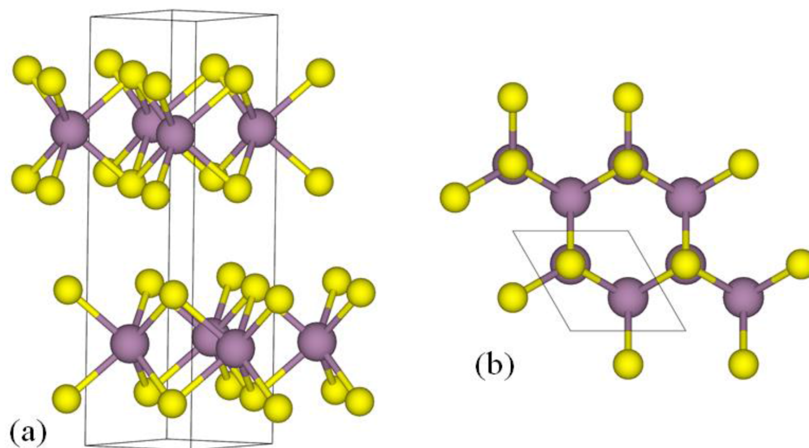

Figure 1. a) Layered structure of MoS_2, space group $P6_3/mmc$, and b) basal projection of the atomic positions. Large purple spheres represent Mo atoms; small yellow spheres, S atoms. The hexagonal primitive unit cell is outlined by solid lines.

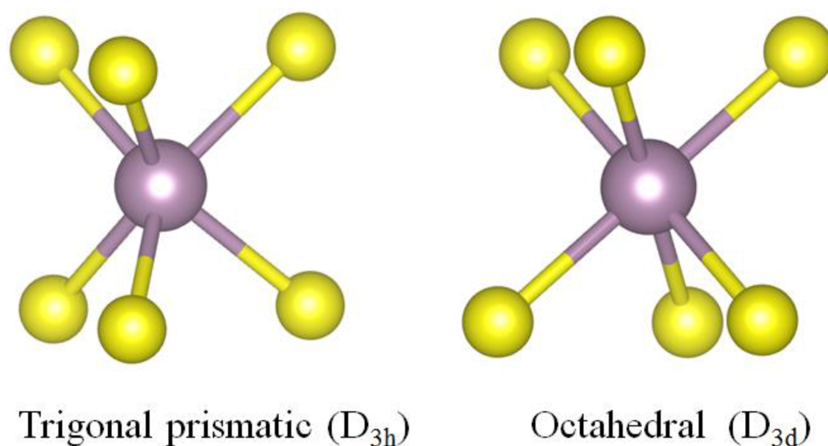

Figure 2. Two polytypes of single MoS_2 layer, depending on Mo atom coordination: a) trigonal prismatic and b) octahedral. Large purple spheres represent Mo atoms; small yellow spheres, S atoms.

3. Energy band structure

Along with the other group-VI layered compounds, 2H-MoS_2 exhibits semiconducting behavior. Measured fundamental indirect band gap of bulk MoS_2 is 1.22 to 1.23 eV, while the direct band gap ranges from 1.74 to 1.77 eV [41,42]. It is illustrative to consider how calculations with different levels of theory approached these values over the past several decades. The energy band structure of bulk MoS_2 is typically computed along the high symmetry directions, revealing the material's electronic properties. Figure 3a shows the first Brillouin zone of MoS_2, with high symmetry points and directions highlighted. Here the reciprocal lattice vectors in the hexagonal structure are given by $b_1 = (2/\sqrt{3}a)\hat{i}$, $b_2 = (1/\sqrt{3}a)(\hat{i} + \sqrt{3}\hat{j}), b_3 = (1/c)k$. Electronic properties of the layered transition metal dichalcogenides have been studied theoretically since the early 1970s. In one

of the earliest works, in 1973 Mattheiss [43] used a nonrelativistic augmented-plane-wave (APW) method to calculate the electronic band structures of several TMDs, including MoS_2. In his early APW calculations, Mattheiss [43] used ad hoc crystal potentials that were derived from the Hartree–Fock–Slater atomic charge densities. In each case, the atomic configurations of the metal and chalcogen atoms were assumed to be $d^n s1$ and $s^2 p^4$, respectively. Additionally, Slater's original free-electron exchange approximation was used. Using group-theoretical methods, single particle energies at the high symmetry points were computed. The indirect band gap between the top of the valence band at the Γ-point and the bottom of the conduction band half-way between the Γ- and K-points (see, for example, Figure 3, and its discussion below), determined by the crystal field splitting of the d-band and hybridization between d_z^2 and d_{xy}, $d_{x^2-y^2}$ subbands, was computed to be 1.156 eV [43]. On the other hand, Huisman et al. [44] and Bullett [45] showed that this ligand-field splitting of d levels in a trigonal prismatic coordination can also be explained as a metal-d–nonmetal-p covalency. Band-structure calculations of similar layered TMDs were also carried out by Bromley et al. [46]. Although these calculations ignored interlayer interactions, they revealed that the electronic structures of these compounds are very similar. These calculations provided significant insight on the electronic properties of layered MoS_2 family materials in general. However, this early approach relies on significant experimental input as well as several postprocessing corrections, limiting their predictive power.

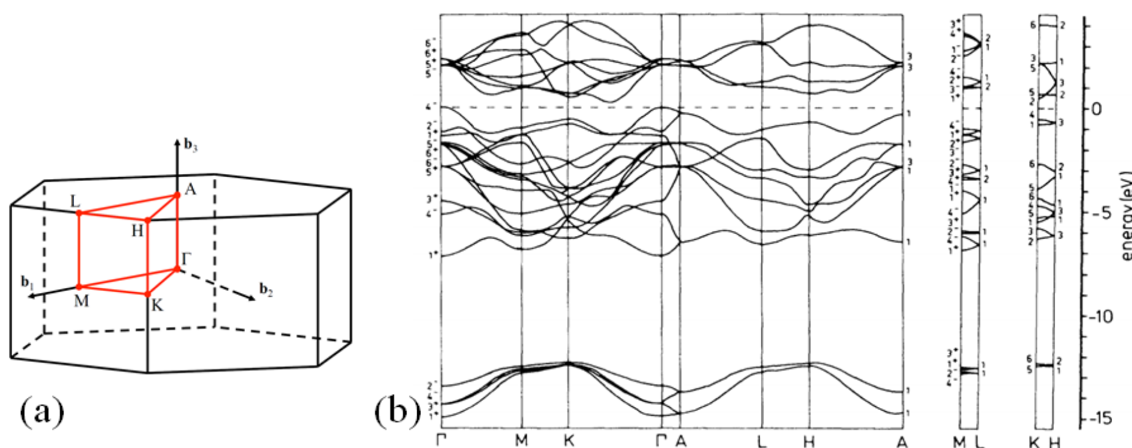

Figure 3. a) First Brillouin zone of MoS_2. b) Band structure of bulk 2H-MoS_2 computed with density functional theory (DFT) within local density approximation (LDA) by Coehoorn et al. [47] Reprinted with permission from Ref. [47]. Copyright 1987 by the American Physical Society.

With the development of density functional theory (DFT), the APW method has been combined with a self-consistent field approach, allowing ab initio type calculations with significantly fewer initial input parameters. In 1987, Coehoorn et al. [47,48] presented a detailed account of electronic properties of bulk MoS_2 (as well as $MoSe_2$ and WSe_2), while directly comparing their calculations to angle-resolved photoelectron spectroscopy measurements. Their approach was based on the local density approximation (LDA) to DFT [49], with spin-orbit interaction included in calculations as a perturbation by adding the $\lambda \mathbf{L} \cdot \mathbf{S}$ term into the Hamiltonian, on top of the zero-order wave functions. The resulting band structure is shown in Figure 3b. The character of the wave functions of the bands was obtained from the site projected Mo and S density of states. The band from –14.8 eV to –12.4 eV is composed mostly of sulfur 4s-states. At the top of the valence band there is the d_z^2 band from about –1.6 to 0 eV. Below –1.6 eV the valence band is derived for the most part from sulfur 4p states

mixed with Mo 4d-states. The conduction band between 0.4 and 3.8 eV also shows considerable Mo4d-S4p covalency. However, the bottom of the conduction band is predominantly of Mo4d character. The indirect band gap has its origin in transitions from the top of the valence band at the Γ-point to the bottom of the conduction band halfway between Γ- and K-points. The direct band gap is located at the K-point in the Brillouin zone. The same qualitative conclusions can be obtained for $MoSe_2$ and WSe_2. Furthermore, Coehoorn et al. [47,48] showed, by directly comparing their results with angle-resolved photoemission experiments, that the augmented-spherical-wave method combined with DFT describes the electronic structure of the MoS_2 family materials very well. However, what the authors also noted was that the computed band gaps were significantly underestimated. The experimentally measured indirect band gaps for $MoSe_2$, MoS_2, and WSe_2 were 1.1, 1.2, and 1.2 eV, respectively [42,50]. The computed band gaps were 30%–50% lower due to the known tendency of local approximations specific to the DFT [51].

It is interesting that these finding were revisited in 2001, when Böker et al. [52], apparently unaware of the previous angle-resolved photoemission studies [47,48], performed similar measurements and calculations with a significantly improved theoretical approach. Although still based on LDA approximation to the DFT, these calculations used nonlocal pseudopotentials [53] to treat electron–ion interactions in the Hamiltonian, and the exchange-correlation energy was taken into account using the Ceperley–Alder [54] form parameterized by Perdew and Zunger [51]. The latter approach dominated electronic structure calculations for nearly 2 decades and only recently has been surpassed by higher order theories. Well aware of the band gap problems of LDA, Böker et al. [52] targeted only the valence band structure of MoS_2 and related compounds. They demonstrated an amazingly good agreement between the theory and experiment for most of the bands, supporting the accuracy of LDA, notwithstanding the description of the excited states.

Similar ab initio calculations were recently performed for 2D MoS2 [18,55]. Calculations commonly use DFT within either LDA or the so-called generalized gradient approximation (GGA) for the exchange-correlation potential. As expected, 2D MoS_2 is a semiconductor with a band gap, which is rather close to that of the 3D analog. There are many similarities with 3D MoS_2; for example, the bands around the band gap are rather flat, as expected from the d character of the electron state. However, an important distinction is that the band gap, which has a value of 1.78 eV, is direct and occurs at the high-symmetry point K. This opens a possibility for band gap modulation by changing the number of layers in the material. In fact, such band gap tuning has been demonstrated recently both theoretically and experimentally by using DFT-GGA calculations along with photoluminescence measurements in MoS_2 layers [18].

The results of the calculations performed by Splendiani et al. [18] are shown in Figure 4, which illustrates the transformation of the MoS_2 band structure with reducing thickness. As in the previous calculations, Splendiani et al. [18] determined bulk MoS_2 to be an indirect band gap semiconductor (Figure 4a). As the number of layers decreases, the indirect band gap inherent to the bulk material becomes larger, while the energy of the direct excitonic transition at the K-point remains virtually unchanged (Figures 4b and 4c). Finally, the energy of the indirect transition moves above that of the direct transition, so that the MoS_2 monolayer is a 2D direct band gap semiconductor (Figure 4d), which should result in enhanced photoluminescence (PL) from the monolayers as compared to the bulk material. The theoretical prediction of indirect to direct band gap transition has been confirmed by experimental observations [13,18,40]. For example, Mak et al. [13] observed an increase in the PL quantum yield from MoS_2 monolayers by more than a factor of 10^4 as compared to the bulk sample.

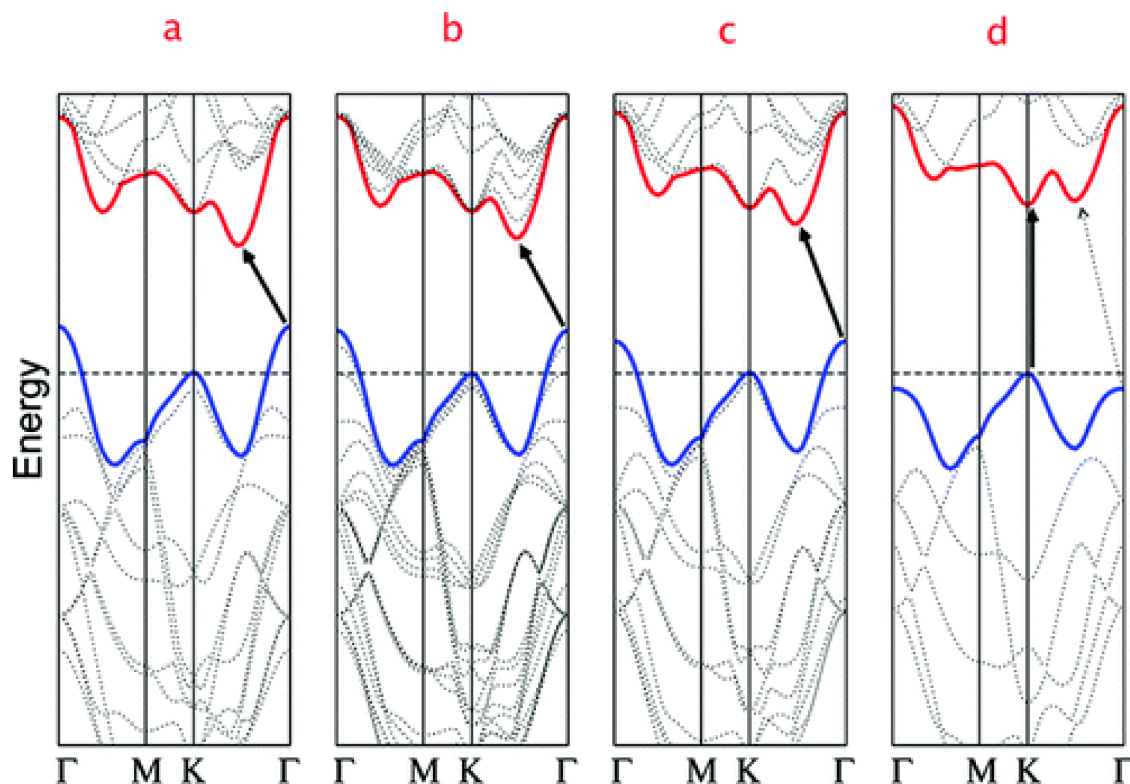

Figure 4. DFT-GGA calculated band structures for **(a)** bulk MoS_2, **(b)** 4-layer MoS_2, **(c)** bilayer MoS_2, and **(d)** monolayer MoS_2. The solid arrows indicate the lowest energy transitions. Reprinted with permission from Ref. [18]. Copyright 2010 American Chemical Society.

This transition from indirect band gap of bulk MoS_2 to the direct band gap of the 2D material originates from the d-character of MoS_2 conduction and valence bands. The conduction band states at the K-point consist primarily of strongly localized d orbitals of Mo atoms. They have relatively weak interlayer coupling, because Mo atoms are located in the middle of the S-Mo-S unit cell, and thus their energies are not affected by the layer thickness. On the contrary, the states at the Γ-point and the point of indirect band gap originate from a hybridization of d orbitals of Mo atoms and p_z orbitals on S atoms and have strong interlayer coupling, and their energies are sensitive to the number of layers. As a result, the indirect band gap gets larger as the number of layers decreases, and for the monolayer geometry it becomes larger than the direct band gap at the K-point. This effect paves the way for engineering electronic structures by modifying the hybridized electronic states. Such capability can lead to the engineering of novel optical processes and holds promise for new applications.

4. Band gap engineering

In the previous paragraphs we discussed the band gap modifications caused by the number of monolayers. Another interesting possibility for bulk and 2D MoS_2 band gap modulation exists in strain engineering [56–62]. Mechanical strain can strongly affect the band structure, carrier effective masses, and transport, optical, and magnetic properties of MoS_2 via changing the distance between the atoms and also the crystal symmetry. Compared with the bulk material, larger strain can be applied to low-dimensional MoS_2 ($>11\%$ [63]) due to its mechanical flexibility, and its properties can be tuned by applied strain, which opens possibilities for developing new tunable electronic devices. Theoretical calculations predict that the band gap of MoS_2 mono- and bilayers

decreases under applied stress, resulting in the change from semiconducting to semimetallic and, ultimately, metallic behavior [58,61,62]. Figures 5a–5g illustrate the effect of strain on the energy band structure and the band gap of MoS_2 single layer. One can see that the calculated band structure undergoes considerable changes under applied stress. The energy band gap gradually decreases with increasing tensile strain, whereas it initially rises and then decreases linearly under applied compressive strain (Figure 5b). It is interesting to note that some theoretical results predict the semiconductor–metal transition for both tensile and compressive strain (at about 8% and 15%, respectively) [61].

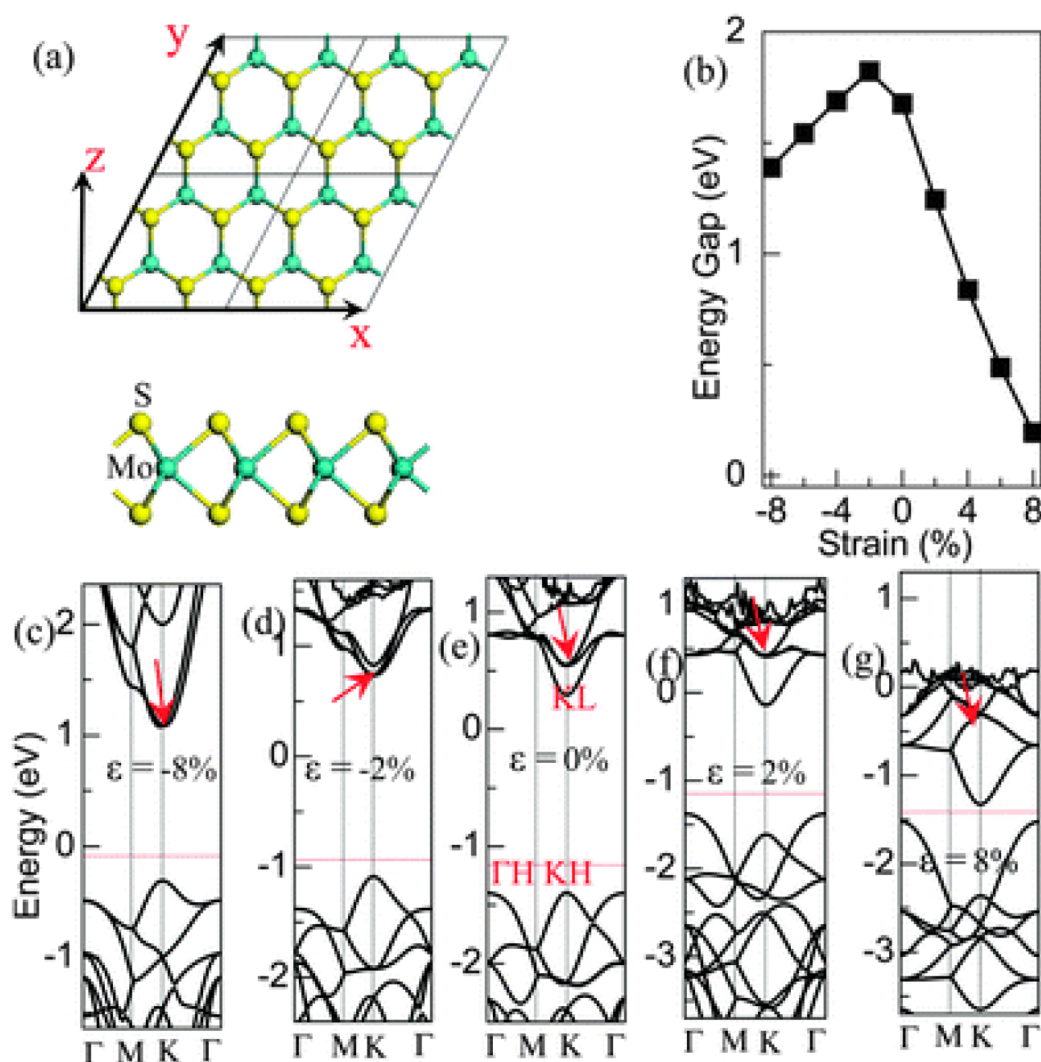

Figure 5. a) Top and side views of MoS_2 monolayer lattice. b) Calculated band gap of monolayer MoS_2 versus isotropic strain. c)–g) Electronic band structure of MoS_2 monolayer under isotropic compressive strain of c) –8% and d) –2%, e) unstrained MoS_2 monolayer, and under isotropic tensile strain of f) 2% and g) 8%. The red dashed line denotes the Fermi level. Red arrows mark a specific band that is the conduction band minimum in the compressive states, but is raised above the conduction band minimum in an unstrained state or under isotropic tensile strain. Reproduced from Ref. [60] with permission of the PCCP Owner Societies. Copyright 2012.

Furthermore, a transition from direct to indirect band gap is predicted for MoS_2 monolayers upon the application of relatively small strain [58,60,61]. As noted above, the MoS_2 monolayer is a semiconductor with a direct gap at the K-point. Upon applied tensile strain, the conduction band minimum remains at the K-point, but the valence band maximum moves from the K-point to the Γ-point, and the material transforms into an indirect gap semiconductor (see Figures 5e–5g). As discussed above, the valence band at the Γ-point originates from the Mo d_z^2 and Sp_z orbitals, unlike the character of the valence band at the K-point. Due to different orbital character, these 2 states respond differently to strain, leading to the changes in the valence band maximum. Strain-induced modulation of the band gap and the transition from an optically direct to an optically indirect material was observed experimentally for MoS_2 mono- and bilayers [59].

Applied strain also affects the effective mass of carriers in MoS_2 [58]. According to the DFT calculations performed by Kang and Li [58], the applied strain influences electrons and holes in different ways. As the strain increases, the effective electron mass decreases for the most part, while the effective hole mass exhibits a nonmonotonic behavior with strain: it initially rises and then decreases. The peak of the hole effective mass at a strain of about 1% is caused by the valence band maximum shifting from the K- to Γ-point during transformation of the band structure. This shift of valence band maximum leads to a dramatic increase in corresponding band dispersion.

The band gap of MoS_2 mono- and bilayers can be also tuned by external electric field applied normally to the sheet [64,65]. DFT calculations indicate that the band gap of MoS_2 bilayers decreases linearly with applied field and vanishes at 2.7 V/nm, when the semiconductor-to-metal transition occurs [64].

5. Carrier mobility

Although carrier mobility limited by phonon scattering in bulk MoS_2 is rather high (200 to 500 $cm^2\ V^{-1}\ s^{-1}$) [66], experimental values reported for MoS_2 monolayers are sometimes considerably lower [4,67,68], which has been attributed to charged impurity scattering mechanism [67–69]. It has been theoretically predicted that electron mobility in 2D semiconductor nanosheets can be enhanced by coating them with high-κ dielectrics owing to suppression of Coulomb scattering [69–71]. Kaasbjerg et al. [69] used a first-principles approach to study electron–phonon interactions and determine intrinsic phonon-limited mobility in n-type MoS_2 monolayers for temperatures $T > 100$ K. Their calculations indicate that at room temperature the mobility should be dominated by optical phonon scattering via intra- and intervalley deformation potential couplings as well as by polar optical scattering on the intravalley LO phonon via the Fr?hlich interaction. The mobility is weakly dependent on the carrier density and follows a

$\mu \sim T^{-\gamma}$ temperature dependence, where the exponent γ depends on the dominant phonon scattering mechanism and is 1.69 at room temperature. Kaasbjerg et al. [69] obtained a theoretical room-temperature mobility value of 410 $cm^2\ V^{-1}\ s^{-1}$ and pointed out that a value close to this intrinsic phonon-limited mobility value could be achieved in MoS_2 monolayers via dielectric engineering that effectively screens static Coulomb scattering.

Very recently, Ma and Jena [71] theoretically analyzed individual scattering mechanisms limiting the mobility in single layers of MoS_2 and concluded that carrier transport depends strongly on the dielectric environment and the impurity density. The authors pointed out that the mobility values reported to date are limited by ionized impurity scattering and are far below the intrinsic mobility in the 2D materials. The true value of intrinsic mobility limited by remote optical phonon scattering may be accessible only in very clean suspended layers. The potential electron mobility in suspended MoS_2 monolayer is assumed to be as high as

10,000 cm^2 V^{-1} s^{-1}. The authors proposed AlN and BN as the best choices for surrounding dielectrics that will allow one to achieve simultaneously high mobility and high gate capacitance values desired for FETs [71].

Experimental studies have confirmed that the use of high-κ oxides as the top-gate dielectrics most likely effectively screens Coulomb scattering on charged impurities and enhances the carrier mobility in 2D MoS_2, although the mechanism is not yet completely understood [5,72–75]. The highest mobility value of 700 cm^2 V^{-1} s^{-1} was reported by Das et al. [75] for a back-gated FET based on 10-nm-thick multilayer MoS_2 flake with Al_2O_3 as a high-κ dielectric and Sc contacts.

There is theoretical and experimental evidence on the crucial role that electrical contacts play in mobility measurements [75–77]. Ab initio DFT calculations for the geometry, bonding, and electronic structure of the contact region have revealed that gold, the most common contact material, forms a tunnel contact to MoS_2 rather than an ohmic one, which suppresses electron injection into MoS_2 [76]. Popov et al. [76] proposed criteria for good contact candidates. In addition to high conductivity and chemical, thermal, and electrical stability, the candidate material must have a high density of delocalized state across the interface at the Fermi level. The promising candidates are transition metals having low work functions providing efficient electron injection into the MoS_2 conduction band and the d orbitals that favorably mix with the Mo4d states. Considering the above, Popov et al. [76] suggested Ti as being the best contact material and Sc and Zr as being less suitable.

Das et al. [75] experimentally demonstrated the existence of the Schottky barriers at the MoS_2/metal contact interfaces for various metals used for the electrical contacts, and that the linear current-drain voltage characteristics usually observed experimentally are due to thermally assisted tunneling through the Schottky barrier rather than due to the ohmic contact. The Schottky barrier heights have been found to be $\sim$230 meV for platinum, $\sim$150 meV for nickel, $\sim$50 meV for titanium, and $\sim$30 meV for scandium electrodes. The metals with lower work function, such as Sc, are considered as the best suited ones for the contacts, providing lower contact resistances and high carrier injection. Das et al. [75] pointed out that the true value of mobility is affected by the presence of the Schottky barriers at the source and drain contacts. The experimental values of mobility in the 10-nm-thick multilayer MoS_2 flake were found to be 21, 90, 125, and 184 cm^2 V^{-1} s^{-1} for Pt, Ni, Ti, and Sc contacts, respectively, which is in a good agreement with the experimental results of Liu et al. [78], who found an effective Schottky barrier at the Ni/MoS_2 interface of $\sim$100 meV or less. The use of Sc contacts with the lowest Schottky barrier provides the highest mobility value. As noted previously, covering the top of the back-gated FET with an Al_2O_3 layer resulted in further improvement of the mobility to 700 cm^2 V^{-1} s^{-1} [75]. A recent study by Pradhan et al. [79] also confirmed the experimental values of carrier mobility in MoS_2-based FETs to be strongly limited by nonohmic contacts. To eliminate the detrimental effect of the contacts and extract the intrinsic carrier mobility in FETs based on multilayered (20 layers thick) MoS_2 on SiO_2/Si, they used a 4-contact configuration and obtained a value of 306.5 cm^2 V^{-1} s^{-1}, which is higher than the value extracted from the same device when using a 2-terminal configuration and is close to the theoretically calculated value of 410 cm^2 V^{-1} s^{-1} [69].

6. Preparation techniques

Due to the weak van der Waals bonds between the successive layers, single MoS_2 layers can be easily obtained by the scotch-tape micromechanical exfoliation technique [5,13,18,80], which is commonly used for the production of graphene [1,81], liquid-phase exfoliation [82–84], lithium-based intercalation [85–90], and plasma [91] or laser [92] thinning of multilayered MoS_2 flakes. The mechanical exfoliation technique yields the highest-quality

monolayers, albeit on a small scale and with low reproducibility, and thus can be used mostly for demonstration of the potential of the 2D material for device applications. Liquid exfoliation methods allow production of relatively larger amounts of 2D material. Simple liquid-phase exfoliation techniques rely on a surfactant to overcome the bonding energy between the layers of the MoS_2 structure, resulting in single or few monolayer thick flakes stabilized by a surfactant coating. Figures 6a and 6b show low- and high-resolution TEM images of a MoS_2 flake obtained by liquid-phase exfoliation, respectively. Hexagonal atomic coordination of atoms in the sheet is clearly seen in the high-resolution image (Figure 6b). This method is simple, can be carried out in ambient conditions, is scalable, and allows the preparation of films, hybrids, and composites. The lack of control over MoS_2 thickness is the main drawback of this approach.

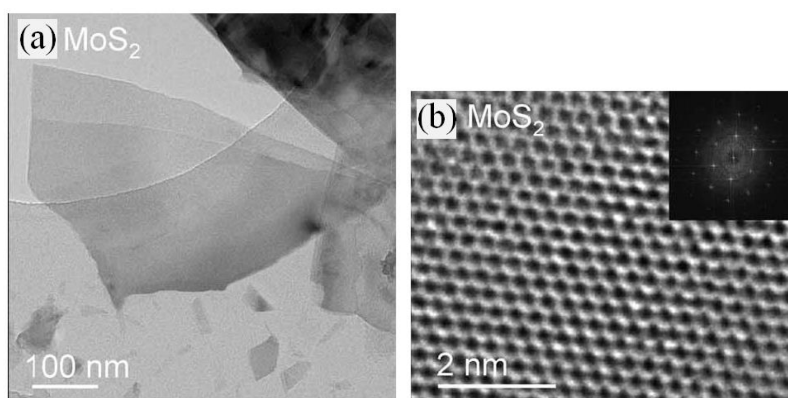

Figure 6. a) Low- and (b) high-resolution TEM images of MoS_2 flake. Reprinted from Ref. [82] with permission. Copyright 2011 American Association for the Advancement of Science.

The lithium intercalation technique is based on the intercalation of lithium species into the layered structure of MoS_2, i.e. the insertion of Li ions between the MoS_2 layers, which facilitates the subsequent exfoliation, as illustrated schematically in Figure 7. For this purpose, MoS_2 powder is soaked in an n-butyl lithium solution, where Li ions intercalate between the layers, forming a near-stoichiometric Li_xMoS_2 compound. The intercalated samples are then immersed in distilled water, where Li reacts with water and evolving hydrogen gas provides exfoliation of monolayer-thick sheets. This method yields almost 100% atomically thin sheets. The limitations of this approach are long lithiation time (about 3 days), high reaction temperature ($\sim$100 °C), submicron size of the ?akes, sensitivity to environmental conditions, and formation of metal nanoparticles and precipitation of Li_2S [86].

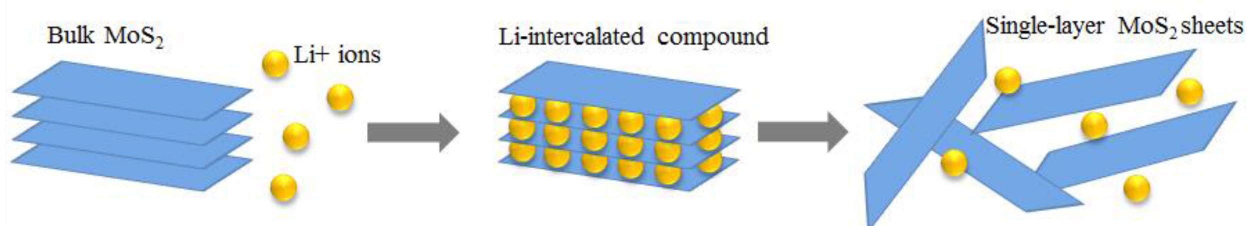

Figure 7. Schematic representation of intercalation of lithium into MoS_2.

The techniques discussed above, however, are hardly suitable for real device fabrication. Large-area layers, high quality, high yield, and precise thickness control are prerequisites for practical devices. Large-area MoS_2 monolayers, conducive for device fabrication, can be grown using various chemical vapor deposition

(CVD) techniques [93–101]. This method allows preparation of continuous single- or few-layer MoS_2 sheets uniform in thickness over a large area (up to centimeters) with good physical properties and is compatible with modern device fabrication technology. High purity MoO_3 and S powders are usually used as Mo and S precursors, respectively, although the use of $MoCl_5$ [98,99] and as the Mo source and thiophenol dissolved in tetrahydrofuran [97] and H_2S [99] as sulfur precursors has been reported. MoS_2 thin layers can be also synthesized via thermolysis of $(NH_4)_2MoS_4$ deposited on a substrate [102]. Si wafers coated with SiO_2 (about 300 nm thick) are generally used as substrates. Benameur et al. [103] found that the optimal thickness for optical detection of single-layer MoS_2 is 270 nm. Figure 8 schematically shows a CVD setup. As seen in the figure, the sources of molybdenum and sulfur are placed inside a hot-wall tube furnace. The substrate is suspended above the boat carrying the Mo source. The growth is achieved at a high temperature (650 to 850 $^\circ$C) in a carrier gas (N_2 or Ar) flow. At a high temperature, sulfur evaporates and reduces MoO_3 to form volatile MoO_{3-x}, which deposits on the substrate and further reacts with sulfur to form a MoS_2 layer. The deposited MoS_2 layers can either be used for further device fabrication or be easily released by removing the substrate in KOH solution and transferred to any other substrate.

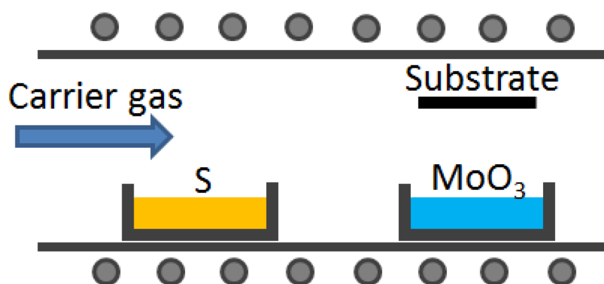

Figure 8. Schematic sketch of a CVD set-up.

One more method well suited for deposition of TMD monolayers is molecular beam epitaxy (MBE). Owing to the precise control over thickness and composition and availability of in situ monitoring and control capabilities, MBE is a perfect technique for deposition of mono- and few-nanolayer-thick films. On the base of MBE, so-called van der Waals epitaxy was achieved in the 1980s [104–107]. van der Waals epitaxy is realizable for the materials with layered structure, such as graphene and TMDs, where the layers are weakly bound by van der Waals forces. As alluded to earlier, these materials have no dangling bonds on the clean surfaces, and the epitaxial growth proceeds with van der Waals forces between successive layers. Ohuchi et al. [106,107] successfully obtained $MoSe_2$ single and multilayers on MoS_2 and SnS_2 substrates using MBE with a conventional Knudsen cell for selenium evaporation and an electrostatically focused electron beam source for Mo evaporation.

van der Waals epitaxy removes the severe lattice matching requirement in regard to the substrate employed since the lattice mismatch can be relieved through the weak van der Waals force and thus makes possible preparation of ultrathin heterostructures (referred to as van der Waals heterostructures [108]) with very abrupt interfaces and low defect density due to the absence of dangling bonds. This approach allows one to grow heterostructures consisting of materials that are selected for their specific properties, rather than for the lattice match, and paves the way to many possibilities for fabricating multilayer heterostructures with novel electronic and optical properties different from their own constituent layers [25,108–110]. For example, using first-principles calculations, Terrones et al. [25,109] demonstrated that by alternating individual layers of different TMD materials (MoS_2, WS_2, WSe_2, and $MoSe_2$) it is possible to obtain bilayer heterostructures with

direct band gaps ranging from 0.79 eV to 1.157 eV, which might be useful for near infrared applications. An interesting feature of these heterostructures is that electrons and holes are physically separated and localized in different layers. The lack of inversion symmetry makes these bilayer heterostructures promising for new valleytronic devices.

van der Waals epitaxy can be also realized via the CVD process [111,112]. Recently, Shi et al. [111] used this approach to obtain MoS_2 flakes on the surface of graphene. Unlike the conventional van der Waals epitaxy, this group used ammonium thiomolybdate ($(NH_4)_2MoS_4$) organic compound as a precursor. The precursor was transported to the graphene surface by a carrier gas at room temperature. Upon postannealing at a relatively low temperature of 400 °C, MoS_2 flakes with lateral sizes of up to several micrometers formed on graphene with their c axis perpendicular to the graphene surface. The large lattice mismatch (~28%) between these 2 materials was relaxed through the weak van der Waals force. Ji et al. [112] grew MoS_2 on a fluorophlogopite mica ($KMg_3AlSi_3O_{10}F_2$) substrate by using low-pressure CVD. With this approach, centimeter-scale high-quality MoS_2 monolayers were synthesized.

Although growth of MoS_2 monolayers by metal-organic CVD (MOCVD) has not yet been reported, it is possible to synthesize MoS_2 by MOCVD using a single-source precursor tert-butyl thiolate $Mo(S\text{-}t\text{-}Bu)_4$ [113]. This well-developed deposition technique is known to provide high quality and uniformity of deposited layers and hence can be considered as a potential candidate for preparation of MoS_2 monolayers of device quality.

Another approach that is capable of providing large-area (~cm^2) sheets of TMDs with controllable thicknesses is sulfurization of ultrathin (5–20 Å) metal or metal oxide films [114–116]. For example, Zhan et al. [114] obtained MoS_2 films by reacting sulfur vapor with Mo predeposited on Si substrates by e-beam evaporation. In this case, the thickness of the MoS_2 layer (from one to few monolayers) was determined by the thickness of the predeposited Mo film. Song et al. [117] used atomic layer deposition (ALD) for predeposition of WO_3 layers followed by sulfurization. In this case, the thickness of WS_2 is easily controlled by keeping track of the number of ALD cycles of WO_3. The ALD method, which is a surface-reaction-controlled variant of CVD, is a very useful technique for deposition of ultrathin layers with near-perfect thickness control because of the layer-by-layer nature of the deposition kinetics. The ALD growth can be described as a 4-step process. First, a gaseous precursor is introduced into the growth chamber and chemisorbs on the substrate surface, and then, at the second step, an inert gas flow removes the unreacted species from the surface. At the third step, the second reactive gas is introduced and chemisorbs on the surface, which is again followed by the inert gas flow to remove the unreacted species, leaving a monolayer of a growing material. This 4-step process can be repeated until a desired thickness is achieved. Scharf et al. [118,119] developed a chemical synthesis route for depositing WS_2 layers down to 8 nm in thickness by ALD. Although we were not able to find reports on TMD monolayers by ALD, this approach is among the most beneficial techniques due to its precise thickness and composition control, large-scale thickness uniformity, and excellent conformity.

7. Device applications

As in the case of graphene, MoS_2 has a wide range of applications. Due to its layered structure, this material is highly anisotropic with excellent nonlinear optical properties [120,121] (second-order nonlinear optical susceptibility $\chi^{(2)} \sim 10^5$ pm/V compared to ~1 pm/V for quartz) and also is a very critical material in tribology as it is an excellent lubricant. The strong covalent in-plane bonding in the layered material paves the way for membranes with mechanical strengths some 30 times higher than that of steel and stability at up to 1100 °C

in an inert atmosphere [63,122], as well as for high-performance flexible electronics [123–125]. Two-dimensional MoS_2 may be used in sensors [80,126,127] and memory [128] and photovoltaic devices [129]. Direct band gap and confinement effects in single-layer MoS_2 makes this material attractive for optoelectronics [130–132], where the tunable and direct band gap would allow a high absorption coefficient and efficient electron–hole pair generation under photoexcitation. Ultrasensitive monolayer-MoS_2 phototransistors with improved device mobility and ON currents have been already demonstrated [127,132]. The devices show a maximum external photoresponsivity of 880 A W^{-1} at a wavelength of 561 nm and a photoresponse in the 400–680 nm range [132].

Figure 9 shows a schematic view of a MoS_2-based phototransistor fabricated by Lee et al. [131]. The device is based on exfoliated MoS_2 flake on a SiO_2 substrate with Au source/drain electrodes, a 50-nm-thick Al_2O_3 layer as a gate dielectric, and transparent indium tin oxide (ITO) top gate electrode. Devices with single-, double-, and triple-layered MoS_2 flakes were fabricated. Due to the thickness dependence of the band gap of 2D MoS_2 (see Figure 4), the phototransistors exhibited sensitivity to different wavelengths as determined by the total layer thickness. The single- and double-layer devices were photosensitive for green light, while the triple-layer one exhibited excellent performance for red light.

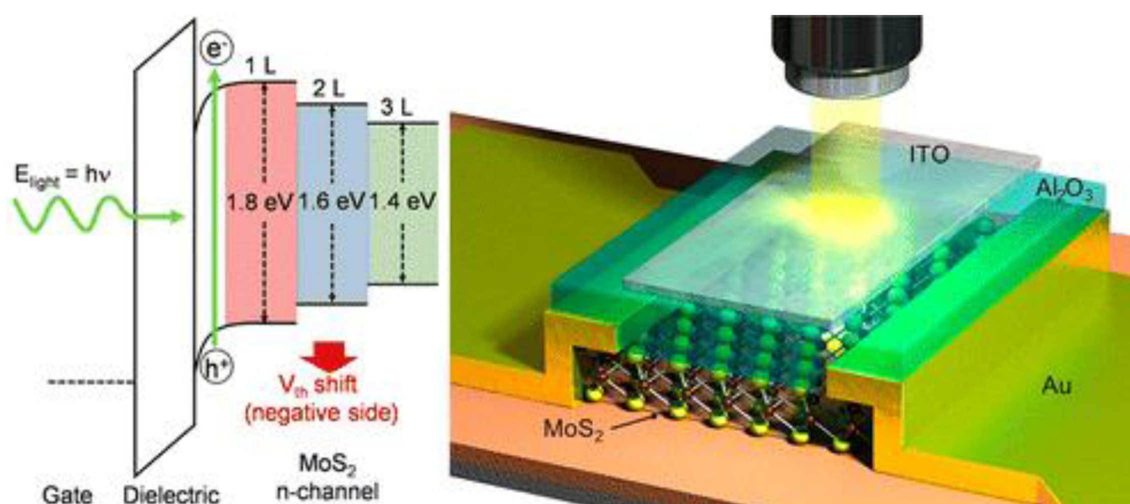

Figure 9. (Left) The schematic band diagram of ITO (gate)/Al_2O_3 (gate dielectric)/single (1 L)-, double (2 L)-, triple (3 L)-layer MoS_2 (n-channel). (Right) Schematic sketch of the phototransistor based on MoS_2 nanosheet. Reprinted with permission from Ref. [131]. Copyright 2012 American Chemical Society.

Since the transistor is at the heart of modern digital electronics, a great deal of attention has been given to monolayer MoS_2-based FETs [5,72,75,78,101,102,123,124]. To compete with Si as a material for digital logic devices, low power consumption, a high ON/OFF current ratio of 10^4 to 10^7, and a band gap of more than 0.4 eV are desirable. Using nonequilibrium Green's function-based quantum transport simulations, Yoon et al. [133] recently performed theoretical studies of the ultimate performance limit of FETs based on MoS_2 monolayers. They predicted a very large ON/OFF current ratio exceeding 10^{10} due to the wide band gap, excellent immunity to short channel effects, and abrupt switching (subthreshold swing as low as 60 mV/dec). In 2011, Radisavljevic et al. [5] fabricated FETs based on a MoS_2 monolayer (6.5 ? thick) obtained by scotch tape-based micromechanical exfoliation, which were transferred on Si substrates covered with 270-nm-thick SiO_2. The degenerately doped Si substrate acted as the back gate. After fabrication of electrical contacts and deposition of 50-nm-thick gold source and drain electrodes, the device was annealed at 200 °C to remove any

resist residue and decrease the contact resistance. A 30-nm-thick layer of high-κ HfO_2 grown by ALD was used as the gate dielectric. The width of the top gate was 4 μm, and the top gate length and the source–gate and gate–drain spacing were 500 nm each. A schematic view of the fabricated FET is shown in Figure 10a. The fabricated devices show behavior typical of the FETs with n-type channels (Figure 10b). A room-temperature current ON/OFF ratio of $>1 \times 10^8$, carrier mobility of $\sim$200 cm^2 V^{-1} s^{-1}, low subthreshold swing (74 mV dec^{-1}), and negligible OFF current (25 fA μm^{-1}) were achieved [5]. For MoS_2-based MOSFETs with channel lengths ranging from 2 μm down to 50 nm, Liu et al. [78] reported superior immunity to short channel effects down to 100 nm channel length and a current on/off ratio of up to $\sim 10^9$.

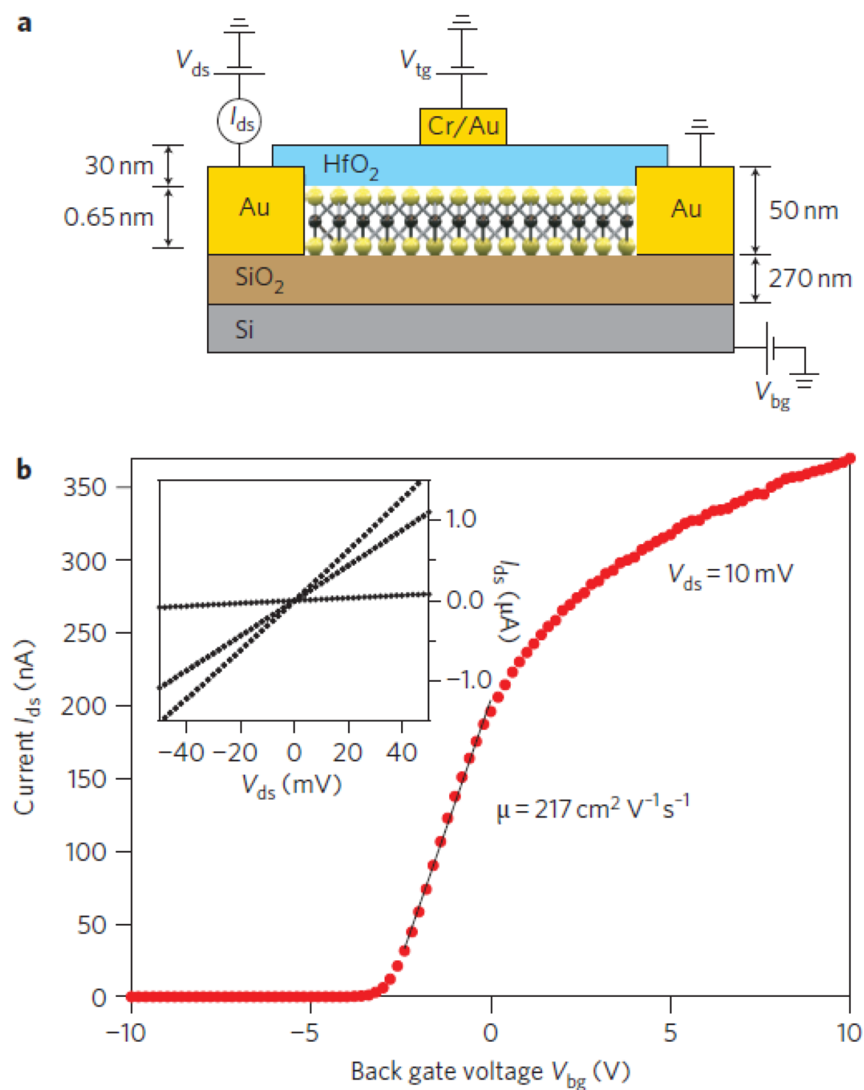

Figure 10. **(a)** Schematic sketch of FET based on MoS_2 monolayer. **(b)** Room-temperature transfer characteristic of the FET shown in **(a)** measured with applied bias voltage V_{ds} = 10 mV. Back gate voltage V_{bg} is applied to the substrate, and the top gate is disconnected. Inset shows I_{ds} vs. V_{ds} plot acquired for V_{bg} values of 0, 1, and 5 V. Reprinted with permission from Ref. [5]. Copyright 2011 Nature Publishing Group.

8. Conclusions and outlook

Two-dimensional materials, particularly the TMD monolayers, are emerging as a new class of materials with a wide range of exciting physical properties with promise for potential applications. Among them, semiconducting MoS_2, together with its cousin materials (WS_2 and $MoSe_2$, MoS_2), is gaining increasing attention owing to an attractive combination of physical properties, which include band gap tunability from 1.2 eV (indirect) for bulk up to 1.9 eV (direct) for monolayer varieties or by alloying (e.g., $Mo_{1-x}W_xS_2$ or $MoS_{2-x}Se_x$), and reasonably high electron mobility (700 cm^2 V^{-1} s^{-1} was demonstrated experimentally and 10,000 cm^2 V^{-1} s^{-1} is predicted). A large amount of theoretical work on MoS_2 and related materials has been undertaken over the years with progressive sophistication. On the experimental front, researchers have focused on several promising directions towards practical applications of 2D MoS_2, in particular the development of field-effect transistors. Thanks to a large band gap of 1.9 eV, field-effect transistors based on monolayer MoS_2 demonstrate high current ON/OFF ratios exceeding 10^8, a low subthreshold swing (74 mV dec^{-1}), and negligible OFF current (25 fA μm^{-1}). Ultrasensitive phototransistors, logic circuits, and amplifiers based on monolayer MoS_2 have also been demonstrated, as well as good output current saturation and high currents. The flexibility, stretchability, and optical transparency of monolayer MoS_2 make it particularly attractive for transparent and flexible electronics.

Although the initial results are indeed very promising, the reported device structures have been fabricated on small-area samples, and further progress towards commercialization requires establishing the technology that would allow fabrication of large-area, electronic-quality 2D sheets. Since the properties of MoS_2 depend strongly on the number of monolayers, techniques providing control over the number of deposited monolayers are highly desirable. The major thrust should be directed towards the development of highly scalable methods that are transferrable to industry, such as chemical vapor deposition and atomic layer deposition. For use in flexible electronics, the major challenge is to find approaches that would produce electronic-quality material at deposition temperatures below 400 °C necessitated by the need for growth directly on transparent plastic substrates. Development of 2D MoS_2-based devices, in particular FETs, for real applications also requires further studies of electrode and gate dielectric materials.

References

[1] Novoselov, K. S.; Geim, A. K.; Morozov, S. V.; Jiang, D.; Zhang, Y.; Dubonos, S. V.; Grigorieva, I. V.; Firsov, A. A. *Science* **2004**, *306*, 666–669.

[2] Schwierz, F. *Nature Nanotechnol.* **2010**, *5*, 487–496.

[3] Dean, C. R.; Young, A. F.; Meric, I.; Lee, C.; Wang, L.; Sorgenfrei, S.; Watanabe, K.; Taniguchi, T.; Kim, P.; Shepard K. L. et al. *Nature Nanotech.* **2010**, *5*, 722–726.

[4] Novoselov, K. S.; Jiang, D.; Schedin, F.; Booth, T. J.; Khotkevich, V. V.; Morozov, S. V.; Geim, A. K. *P. Natl. Acad. Sci. USA* **2005**, *102*, 10451–10453.

[5] Radisavljevic, B.; Radenovic, A.; Brivio, J.; Giacometti, V.; Kis, A. *Nature Nanotechnol.* **2011**, *6*, 147–150.

[6] Fang, H.; Chuang, S; Chang, T. C.; Takei, K.; Takahashi, T.; Javey, A. *Nano Lett.* **2012**, *12*, 3788–3792.

[7] Liu, W.; Kang, J.; Sarkar, D.; Khatami, Y.; Jena, D.; Banerjee, K. *Nano Lett.* **2013**, *13*, 1983–1990.

[8] Friend, R. H.; Yoffe, A. D. *Adv. Phys.* **1987**, *36*, 1–94.

[9] Thurston, T. R.; Wilcoxon, J. P. *J. Phys. Chem. B* **1999**, *103*, 11–17.

[10] Abrams, B. L.; Wilcoxon, J. P. *Crit. Rev. Solid State Mater. Sci.* **2005**, *30*, 153–182.

[11] Wilcoxon, J. P.; Newcomer, P. P.; Samara, G. A. *J. Appl. Phys.* **1997**, *81*, 7934–7944.

[12] Tenne, R.; Redlich, M. *Chem. Soc. Rev.* **2010**, *39*, 1423–1434.

[13] Mak, K. F.; Lee, C.; Hone, J.; Shan, J.; Heinz, T. F. *Phys. Rev Lett.* **2010**, *105*, 136805.

[14] Matte, H. S. S. R.; Gomathi, A.; Manna, A. K.; Late, D. J.; Datta, R.; Pati, S. K.; Rao, C. N. R. *Angew. Chem. Int. Ed.* **2010**, *49*, 4059–4062.

[15] Lee, C.; Li, Q.; Kalb, W.; Liu, X. Z.; Berger, H.; Capick, R. W.; Hone, J. *Science* **2010**, *328*, 76–79.

[16] Kam, K. K.; Parkinson, B. A. *J. Phys. Chem.* **1982**, *86*, 463–467.

[17] Chhowalla, M.; Shin, H. S.; Eda, G.; Li, L. J.; Loh, K. P.; Zhang, H. *Nature Chemistry* **2013**, *5*, 263–275.

[18] Splendiani, A.; Sun, L.; Zhang, Y.; Li, T.; Kim, J.; Chim, C. Y.; Galli, G.; Wang, F. *Nano Lett.* **2010**, *10*, 1271–1275.

[19] Lebegue, S.; Eriksson, O. *Phys. Rev. B* **2009**, *79*, 115409.

[20] Kuc, A., Zibouche, N.; Heine, T. *Phys. Rev. B* **2011**, *83*, 245213.

[21] Ellis, J. K.; Lucero, M. J.; Scuseria, G. E. *Appl. Phys. Lett.* **2011**, *99*, 261908.

[22] Kumar, A.; Ahluwalia, P. K. *Eur. Phys. J. B* **2012**, *85*, 186–187.

[23] Kadantsev, E. S.; Hawrylak, P. *Solid State Commun.* **2012**, *152*, 909–913.

[24] Jin, W.; Yeh, P. C.; Zaki, N.; Zhang, D.; Sadowski, J. T.; Al-Mahboob, A.; van der Zande, A. M.; Chenet, D. A.; Dadap, J. I.; Herman, I. P. et al. *Phys. Rev. Lett.* **2013**, *111*, 106801.

[25] Terrones, H.; Terrones, M. *J. Mater. Res.* **2014**, *29*, 373–377.

[26] Chen, Y.; Xi, J.; Dumcenco, D. O.; Liu, Z.; Suenaga, K.; Wang, D.; Shuai, Z.; Huang, Y. S.; Xie. L. *ACS Nano* **2013**, *7*, 4610–4615.

[27] Kosmider, K.; Fernandez-Rossier, J. *Phys. Rev. B* **2013**, *87*, 075451.

[28] Bao, W.; Cai, X.; Kim, D.; Sridhara, K.; Fuhrer, M. S. *Appl. Phys. Lett.* **2013**, *102*, 042104.

[29] Radisavljevic, B., Whitwick, M. B.; Kis, A. *ACS Nano* **2011**, *5*, 9934–9938.

[30] Wang, H.; Yu, L.; Lee, Y. H.; Shi, Y.; Hsu, A.; Chin, M. L.; Li, L. J.; Dubey, M.; Kong, J.; Palacios, T. *Nano Lett.* **2012**, *12*, 4674–4680.

[31] Radisavljevic, B.; Whitwick, M. B.; Kis, A. *Appl. Phys. Lett.* **2012**, *101*, 043103.

[32] Lembke, D.; Kis, A. *ACS Nano* **2012**, *6*, 10070–10075.

[33] Kaul, A. B. *J. Mater. Res.* **2014**, *29*, 348–352.

[34] Chhowalla, M.; Shin, H. S.; Eda, G.; Li, L. J.; Loh, K. P.; Zhang, H. *Nature Chemistry* **2013**, *5*, 263–275.

[35] Jariwala, D.; Sangwan, V. K.; Lauhon, L. J.; Marks, T. J.; Hersam, M. C. *ACS Nano* **2014**, *8*, 1102–1120.

[36] Podberezskaya, N. V.; Magarill, S. A.; Pervukhina, N. V.; Borisov, S. V. *J. Struct. Chem.* **2001**, *42*, 654–681.

[37] Dickinson, R. G.; Pauling, L. *J. Am. Chem. Soc.* **1923**, *45*, 1466–1471.

[38] Wakabayashi, N.; Smith, H. G.; Nicklow, R. M. *Phys. Rev. B* **1975**, *12*, 659–665.

[39] Chhowalla, M.; Shin, H. S.; Eda, G.; Li, L. J.; Loh, K. P.; Zhang, H. *Nature Chemistry* **2013**, *5*, 263–275.

[40] Eda, G.; Yamaguchi, H.; Voiry, D.; Fujita, T.; Chen, M.; Chhowalla, M. *Nano Lett.* **2011**, *11*, 5111–5116.

[41] Baglio, J. A.; Calabrese, G. S.; Kamieniecki, E.; Kershaw, R.; Kublia, C. P.; Ricco, A. J. *J. Electrochem. Soc.* **1982**, *129*, 1461–1472.

[42] Kam, K. K.; Parkinson, B. A.; Kam, K. K.; Parkinson, B. A. *J. Phys. Chem.* **1982**, *86*, 463–467.

[43] Mattheiss, L. F. *Phys. Rev. B* **1973**, *8*, 3719–3725.

[44] Huisman, R.; de Jonge, R.; Haas, C.; Jellinek, F. *J. Solid State Chem.* **1971**, *3*, 56–59.

[45] Bullett, D. W. *J. Phys. C* **1978**, *11*, 4501–4508.

[46] Bromley, R. A.; Murray, R. B.; Yoffe, A. D. *J. Phys. C* **1972**, *5*, 759–764.

[47] Coehoorn, R.; Haas, C.; Dijkstra, J.; Flipse, C.; De Groot, R. A.; Wold, A. *Phys. Rev. B* **1987**, *35*, 6195–6199.

[48] Coehoorn, R.; Haas, C.; De Groot, R. A. *Phys. Rev. B* **1987**, *35*, 6203–6210.

[49] Hedin, L.; Lundquist, B. I. *J. Phys. C* **1971**, *4*, 2064–2070.

[50] Karn, K. K.; Chang, C. L.; Lynch, D. W. *J. Phys. C* **1984**, *17*, 4031–4037.

[51] Perdew, J. P.; Zunger, A. *Phys. Rev. B* **1981**, *23*, 5048–5057.

[52] Boker, T.; Severin, R.; Muller, A.; Janowitz, C.; Manzke, R.; Voß, D.; Kruger, P.; Mazur, A.; Pollmann, J. *Phys. Rev. B* **2001**, *64*, 235305.

[53] Bachelet, G. B.; Hamann, D. R.; Schluter, M. *Phys. Rev. B* **1982**, *26*, 4199–4210.

[54] Ceperly, D. M.; Alder, B. J. *Phys. Rev. Lett.* **1980**, *45*, 566–571.

[55] Lebegue, S.; Eriksson, O. *Phys. Rev. B* **2009**, *79*, 115409.

[56] Kou, L.; Frauenheim, T.; Chen, C. *J. Phys. Chem. Lett.* **2013**, *4*, 1730–1736.

[57] Guo, H.; Lu, N.; Wang, L.; Wu, X.; Zeng, X. C. *J. Phys. Chem. Lett. C* **2014**, *118*, 7242–7249.

[58] Kang, J.; Li, J. In *MoS_2, Lecture Notes in Nanoscale Science and Technology 21*; Wang, Z. M., Ed., Springer International Publishing: Cham, Switzerland, 2014.

[59] Conley, H. J.; Wang, B.; Ziegler, J. I.; Haglund, R. F.; Pantelides, S. T.; Bolotin, K. I. *Nano Lett.* **2013**, *13*, 3626–3630.

[60] Lu, P.; Wu, X.; Guo, W.; Zeng, X. C. *Phys. Chem. Chem. Phys.* **2012**, *14*, 13035–13039.

[61] Scalise, E.; Houssa, M.; Pourtois, G.; Afanasev, V.; Stesmans, A. *Nano Res.* **2012**, *5*, 43–49.

[62] Yun, W. S.; Han, S. W.; Hong, S. C.; Kim, I. G.; Lee, J. D. *Phys. Rev. B* **2012**, *85*, 033305.

[63] Bertolazzi, S.; Brivio, J.; Kis, A. *ACS Nano* **2011**, *5*, 9703–9709.

[64] Ramasubramaniam, A.; Naveh, D.; Towe, E. *Phys. Rev. B* **2011**, *84*, 205325.

[65] Newaz, A. K. M.; Prasai, D.; Ziegler, J. I; Caudel, D.; Robinson, S.; Haglund, R. F. Jr.; Bolotin, K. I. *Solid State Commun.* **2013**, *155*, 49–52.

[66] Fivaz, R.; Mooser, E. *Phys. Rev.* **1967**, *163*, 743–755.

[67] Ghatak, S.; Pal, A. N.; Ghosh, A. *ACS Nano* **2011**, *5*, 7707–7712.

[68] Jariwala, D.; Sangwan, V. K.; Late, D. J.; Johns, J. E.; Dravid, V. P.; Marks, T. J.; Lauhon, L. J.; Hersam, M. C. *Appl. Phys. Lett.* **2013**, *102*, 173107.

[69] Kaasbjerg, K.; Thygesen, K. S.; Jacobsen, K. W. *Phys. Rev. B* **2012**, *85*, 115317.

[70] Jena, D.; Konar, A. *Phys. Rev. Lett.* **2007**, *98*, 136805.

[71] Ma, N.; Jena, D. *Phys. Rev. X* **2014**, *4*, 011043.

[72] Liu, H.; Ye, P. D. *IEEE Electron Device Lett.* **2012**, *33*, 546–548.

[73] Liu, H.; Xu, K.; Zhang, X. J.; Ye, P. D. *Appl. Phys. Lett.* **2012**, *100*, 152115.

[74] Radisavljevic, B.; Kis, A. *Nat. Mater.* **2013**, *12*, 815–822.

[75] Das, S.; Chen, H. Y.; Penumatcha, A. V.; Appenzeller, J. *Nano Lett.* **2013**, *13*, 100–113.

[76] Popov, I.; Seifert, G.; Tomanek, D. *Phys. Rev. Lett.* **2012**, *108*, 156802.

[77] Liu, H.; Si, M.; Najmaei, S.; Neal, A. T.; Du, Y.; Ajayan, P. M.; Lou, L.; Ye, P. D. *Nano Lett.* **2013**, *13*, 2640–2646.

[78] Liu, H.; Neal, A. T.; Ye, P. D. *ASC Nano* **2012**, *6*, 8563–8569.

[79] Pradhan, N. R.; Rhodes, D.; Zhang, Q.; Talapatra, S.; Terrones, M.; Ajayan, P. M.; Balicas, L. *Appl. Phys. Lett.* **2013**, *102*, 123105.

[80] Li, H.; Wu, J.; Yin, Z.; Zhang, H. *Acc. Chem. Res.* **2014**, *47*, 1067–1075.

[81] Novoselov, K. S.; Geim, A. K.; Morozov, S. V.; Jiand, D.; Zhang, Y.; Dubonos, S. V.; Grigorieva, I. V.; Firsov, A. A. *Science* **2004**, *306*, 666–669.

[82] Coleman, J. N.; Lotya, M.; O'Neill, A.; Bergin, S. D.; King, P. J.; Khan, U.; Young, K.; Gaucher, A.; De, S.; Smith, R. J. et al. *Science* **2011**, *331*, 568–571.

[83] Lee, K.; Kim, H. Y.; Lotya, M.; Coleman, J. N.; Kim, G. T.; Duesberg, G. S. *Adv. Mater.* **2011**, *23*, 4178–4182.

[84] Smith, R. J.; Ronan, J.; King, P. J.; Lotya, M.; Wirtz, C.; Khan, U.; De, S.; O'Neill, A.; Duesberg, G. S.; Grunlan, J. C. et al. *Adv. Mater.* **2011**, *23*, 3944–3948.

[85] Benavente, E.; Santa Ana, M. A.; Mendizabal, F.; Gonzalez, G. *Coordin. Chem. Rev.* **2002**, *224*, 87–109.

[86] Joensen, P.; Frindt, R. F.; Morrison, S. R. *Mater. Res. Bull.* **1986**, *21*, 457–461.

[87] Schumacher, A.; Scandella, L.; Kruse, N.; Prins, R. *Surf. Sci. Lett.* **1993**, *289*, L595–L598.

[88] Jimenez Sandoval, S.; Yang, D.; Frindt, R. F.; Irwin, J. C. *Phys. Rev. B* **1991**, *44*, 3955–3961.

[89] Zeng, Z. Y.; Yin, Z. Y.; Huang, X.; Li, H.; He, Q. Y.; Lu, G.; Boey, F.; Zhang, H. *Angew. Chem. Int. Ed.* **2011**, *50*, 11093–11097.

[90] Zheng, J.; Zhang, H.; Dong, S.; Liu, Y.; Nai, C. T.; Shin, H. S.; Jeong, H. Y.; Liu, B; Loh, K. P. *Nature Communications* **2014**, *5*, 2995–2999.

[91] Liu, Y.; Nan, H.; Wu, X.; Pan, W.; Wang, W.; Bai, J.; Zhao, W.; Sun, L.; Wang, X.; Ni, Z. *ACS Nano* **2013**, *7*, 4202–4207.

[92] Castellanos-Gomez, A.; Barkelid, M.; Goossens, A. M.; Calado, V. E.; van der Zant, H. S. J.; Steele, G. A. *Nano Lett.* **2012**, *12*, 3187–3190.

[93] Lee, Y. H.; Zhang, X. Q.; Zhang, W.; Chang, M. T.; Lin, C. T.; Chang, K. D.; Yu, Y. C.; Wang, J. T. W.; Chang, C. S.; Li, L. J. et al. *Adv. Mater.* **2012**, *24*, 2320–2325.

[94] Zande, A. M.; Huang, P. Y.; Chenet, D. A.; Berkelbach, T. C.; You, Y.; Lee, G. H.; Heinz, T. F.; Reichman, D. R.; Muller, D. A.; Hone J. *Nat. Mater.* **2013**, *12*, 554–561.

[95] Yu, Y.; Li, C.; Liu, Y.; Su, L.; Zhang, Y.; Cao, L. *Sci. Rep.* **2013**, *3*, 1866–1870.

[96] Najmaei, S.; Liu, Z.; Zhou, W.; Zou, X.; Shi, G.; Lei, S.; Yakobson, B. I.; Idrobo, J. C.; Ajayan, P. M.; Lou, J. *Nat. Mater.* **2013**, *12*, 754–759.

[97] Mann, J.; Ma, Q.; Odenthal, P. M.; Isarraraz, M.; Le, D.; Preciado, E.; Barroso, D.; Yamaguchi, K.; von Son Palacio, G.; Nguyen, A. et al. *Adv. Mater.* **2014**, *26*, 1399–1404.

[98] Yu, Y.; Li, C.; Liu, Y.; Su, L.; Zhang, Y.; Cao, L. *Scientific Reports* **2013**, *3*, 1866.

[99] Endler, I.; Leonhardt, A.; Konig, U.; van den Berg, H.; Pitschke, W.; Sottke, V. *Surface and Coatings Technology* **1999**, *120–121*, 482–488.

[100] Wang, X. H.; Feng, H. B.; Wu, Y. M.; Jiao, L. *J. Am. Chem. Soc.* **2013**, *135*, 5304–5307.

[101] Sharma, D.; Amani, M.; Motayed, A.; Shah, P. B; Birdwell, A. G.; Najmaei, S.; Ajayan, P. M.; Lou, J.; Dubey, M.; Li, Q. et al. *Nanotechnology* **2014**, *25*, 155702.

[102] Liu, K. K.; Zhang, W.; Lee, Y. H.; Lin, Y. C.; Chang, M. T.; Su, C. Y.; Chang, C. S.; Li, H.; Shi, Y.; Zhang, H. et al. *Nano Lett.* **2012**, *12*, 1538–1544.

[103] Benameur, M.; Radisavljevic, B.; Sahoo, S.; Berger, H.; Kis, A. http://lanl.arxiv.org/abs/1006.1048v1, 2010.

[104] Koma, A.; Sunouchi, K.; Miyajima, T. *J. Vac. Sci. Technol. B* **1985**, *3*, 724–729.

[105] Koma, A.; Yoshimura, K. *Surf. Sci.* **1986**, *174*, 556–560.

[106] Ohuchi, F. S.; Shimada, T.; Parkinson, B. A. *J. Cryst. Growth* **1991**, *111*, 1033–1037.

[107] Ohuchi, F. S.; Parkinson, B. A.; Ueno, K.; Koma, A. *J. Appl. Phys.* **1990**, *68*, 2168–2172.

[108] Geim, A. K.; Grigorieva, I. V. *Nature* **2013**, *499*, 419–423.

[109] Terrones, H.; Lopez-Urias, F.; Terrones, M. *Sci. Rep.* **2013**, *3*, 1549–1555.

[110] Lu, N.; Guo, H.; Wang, L.; Wu, X.; Zeng, X. C. *Nanoscale* **2014**, *6*, 4566–4570.

[111] Shi, Y.; Zhou, W.; Lu, A. Y.; Fang, W.; Lee, Y. H.; Hsu, A. L.; Kim, S. M.; Kim, K. K.; Yang, H. Y.; Li, L. J. et al. *Nano Lett.* **2012**, *12*, 2784–2791.

[112] Ji, Q.; Zhang, Y.; Gao, T.; Zhang, Y.; Ma, D.; Liu, M.; Chen, Y.; Qiao, X.; Tan, P. H.; Kan, M. et al. *Nano Lett.* **2013**, *13*, 3870–3877.

[113] Cheon, J.; Gozum, J. E.; Girolami, G. S. *Chem. Mater.* **1997**, *9*, 1847–1853.

[114] Zhan, Y.; Liu, Z.; Najmaei, S.; Ajayan, P. M.; Lou, J. *Small* **2012**, *8*, 966–971.

[115] Ellas, A. L.; Perea-Lopez, N.; Castro-Beltran, A.; Berkdemir, A.; Lv, R.; Feng, S.; Long, A. D.; Hayashi, T.; Kim, Y. A.; Endo, M. et al. *ACS Nano* **2013**, *7*, 5235–5242.

[116] Gutierrez, H. R.; Perea-Lopez, N.; Ellas, A. L.; Berkdemir, A.; Wang, B.; Lv, R.; Lopez-Urlas, F.; Crespi, V. H.; Terrones, H.; Terrones, M. *Nano Lett.* **2013**, *13*, 3447–3454.

[117] Song, J. G.; Park, J.; Lee, W.; Choi, T.; Jung, H.; Lee, C. W.; Hwang, S. H.; Myoung, J. M.; Jung, J. H.; Kim, S. H. et al. *ACS Nano* **2013**, *7*, 11333–11340.

[118] Scharf, T. W.; Prasad, S. V.; Dugger, M. T.; Kotula, P. G.; Goeke, R. S.; Grubbs, R. K. *Acta Mater.* **2006**, *54*, 4731–4743.

[119] Scharf, T. W.; Prasad, S. V.; Mayer, T. M.; Goeke, R. S.; Dugger, M. T. *J. Mater. Res.* **2004**, *19*, 3443–3446.

[120] Kumar, N; Najmaei, S; Cui, Q; Ceballos, F; Ajayan, P. M.; Lou, J; Zhao, H. *Phys. Rev. B* **2013**, *87*, 161403.

[121] Malard, L. M.; Alencar, T. V.; Barboza, A. M.; Mak, K. F.; de Paula. A. M. *Phys. Rev. B* **2013**, *87*, 201401.

[122] Brivio, J.; Alexander, D. T. L.; Kis, A. *Nano Lett.* **2011**, *11*, 5148–5153.

[123] Chang, H. Y.; Yang, S.; Lee, J.; Tao, L.; Hwang, W. S. *ACS Nano* **2013**, *7*, 5446–5452.

[124] Salvatore, G. A.; Munzenrieder, N.; Barraud, C.; Petti, L.; Zysset, C.; Buthe, L.; Ensslin, K.; Troster, G. *ACS Nano* **2013**, *7*, 8809–8813.

[125] Chang, H. Y.; Yang, S.; Lee, J.; Tao, L.; Hwang, W. S.; Jena, D.; Lu, N.; Akinwande, D. *ACS Nano* **2013**, *7*, 5446–5452.

[126] Li, H.; Yin, Z. Y.; He, Q. Y.; Huang, X.; Lu, G.; Fam, D. W. H.; Tok, A. I. Y.; Zhang, Q.; Zhang, H. *Small* **2012**, *8*, 63–67.

[127] Zhu, C.; Zeng, Z.; Li, H.; Li, F.; Fan, C.; Zhang, H. *J. Am. Chem. Soc.* **2013**, *135*, 5998–6001.

[128] Bertolazzi, S.; Krasnozhon, D.; Kis, A. *ACS Nano* **2013**, *7*, 3246–3252.

[129] Gourmelon, E.; Lignier, O.; Hadouda, H.; Couturier, G.; Bernede, J. C.; Tedd, J.; Pouzed, J.; Salardenne, J. *Sol. Energy Mater. Sol. Cells* **1997**, *46*, 115–121.

[130] Yin, Z. Y.; Li, H.; Li, H.; Jiang, L.; Shi, Y. M.; Sun, Y. H.; Lu, G.; Zhang, Q.; Chen, X. D.; Zhang, H. *ACS Nano* **2012**, *6*, 74–80.

[131] Lee, H. S.; Min, S. W.; Chang, Y. G.; Park, M. K.; Nam, T.; Kim, H.; Kim, J. H.; Ryu, S.; Im, S. *Nano Lett.* **2012**, *12*, 3695–3700.

[132] Lopez-Sanchez, O.; Lembke, D.; Kayci, M.; Radenovic, A.; Kis, A. *Nature Nanotechnology* 2013, *8*, 497–501.

[133] Yoon, Y.; Ganapathi, K.; Salahuddin, S. *Nano Lett.* **2011**, *11*, 3768–3773.